Journal of Physics D:
Applied Physics

PAPER

Terahertz high-gain leaky-wave antenna utilizing valley topological photonic crystals with line defects

To cite this article: Haolong Wang *et al* 2025 *J. Phys. D: Appl. Phys.* **58** 215104

IOP Publishing Journal of Physics D: Applied Physics
J. Phys. D: Appl. Phys. **58** (2025) 215104 (10pp) https://doi.org/10.1088/1361-6463/add023

Terahertz high-gain leaky-wave antenna utilizing valley topological photonic crystals with line defects

Haolong Wang[1], Hongyu Shi[1,*], Wei E I Sha[2], Zhihao Lan[3], Fei Gao[2], Xiaoming Chen[1] and Anxue Zhang[1]

[1] School of Information and Communications Engineering, Xi'an Jiaotong University, Xi'an 710049, People's Republic of China
[2] State Key Laboratory of Modern Optical Instrumentation, College of Information Science and Electronic Engineering, Zhejiang University, Hangzhou, People's Republic of China
[3] Department of Electronic and Electrical Engineering, University College London, Torrington Place, London, United Kingdom

E-mail: hongyushi@xjtu.edu.cn

Received 17 March 2025, revised 18 April 2025
Accepted for publication 24 April 2025
Published 2 May 2025

Abstract

By utilizing topological edge states in the fast-wave region and eliminating back reflections, topological photonic crystal (TPC)-based antennas emerge as a promising research direction. In this paper, a leaky-wave topological antenna (TA) is designed using a valley TPC-based topological waveguide (TW) with line defects. We theoretically calculate the antenna's radiation direction and propagation constant, elucidating its radiation mechanism, and verified the results through simulations, which demonstrate excellent agreement with the theoretical predictions. Operating between 0.382 and 0.426 THz, the TA exhibits frequency-scanning capabilities and robustness against fabrication defects. The transverse electric and magnetic (TEM) horn antenna, compatible with the TW, was utilized to refine the beam shape from a fan-shaped beam to a pencil beam, enhancing its suitability for practical application scenarios. The impact of TEM horn antennas with aperture angles of 30°, 40°, and 50° on the performance and radiation patterns of the TA is evaluated. The simulation results indicate that the designed TA demonstrates excellent performance, achieving a maximum realized gain of 21.7 dBi, an aperture efficiency of 63.7%, and a total efficiency exceeding 80%, with a peak value of 95%. This work simulates a leaky-wave valley TA design operating near the 0.410 THz atmospheric window, advancing the theoretical study of TPC radiation, accelerating their engineering applications, and highlighting their significant potential for practical use.

Keywords: topological photonic crystal (TPCs), line defect edge states, leaky-wave antenna, terahertz (THz), topological waveguides and antennas

1. Introduction

The terahertz (THz) frequency band, located between the microwave and optical regions, has emerged as a key focus in electromagnetic (EM) research, offering applications in radar, remote sensing, secure communications, and medical diagnostics [1–5]. Its unique properties present immense potential but also significant challenges, such as the lack of high-power sources, sensitivity to defects and sharp bends [6], Ohmic losses in waveguides [7], and limited bandwidth caused by dispersion [8]. Addressing these issues demands the development of robust, efficient, and broadband THz devices and antennas [9]. To address these challenges, topological

* Author to whom any correspondence should be addressed.

photonic crystals (TPCs) and their edge states have gained significant attention in EM due to their unique properties, such as defect and sharp bend immunity [10, 11], low-loss edge-confined energy [12] and chirality-protected minimal back-scattering [13–15]. These attributes make topological waveguides (TWs) a promising solution for challenges in the THz frequency band.

TPCs are classified by dimensionality into one-dimensional [16, 17], two-dimensional [18, 19], and higher-order [20] structures, with two-dimensional all-dielectric TPCs being the most studied. Among these, spin TPCs [10, 21] and valley TPCs [11, 22, 23] stand out for their distinct physical characteristics. Valley TPCs, in particular, achieve topological edge states by breaking spatial inversion symmetry, which induces opposite valley Chern numbers without requiring an external magnetic field, making them highly suitable for practical applications [24]. Recent studies have uncovered novel physical states in TPCs, including corner states [25–28], spatially extended defect states [21, 29], and large-area transmission states [30–33], further expanding their research scope.

The directional transmission property of TWs eliminates backward reflection, combined with their fast-wave operation simplifies the design of topological antennas (TAs) [34, 35]. Existing TAs, such as acoustic TA [36], all-dielectric TA [37], and reciprocal TPC-based radiation surfaces [38], achieve forward or backward radiation through optimized designs. However, most designs rely on Chern TPCs, which necessitate external magnetic fields, thereby limiting their practicality. In contrast, valley TPCs offer a more practical alternative due to their ability to achieve topological states without external fields. Edge-emitting and broadside radiation arrays have also been explored [14, 39, 40], showcasing directional tunability, frequency-scanning, and defect robustness. Recent studies on THz TPCs have proposed innovative devices, including flexible multiplexer chips [9], adjustable corner states [26], and power dividers with arbitrary ratios [41]. TPCs are also advancing THz on-chip communication systems, offering high speed, low loss, and low bit error rates [6, 37, 42, 43]. For wireless transmission, TAs with operating frequencies near the atmospheric window are ideal for satellite internet systems, as they help minimize transmission losses [44]. In conclusion, designing high-efficiency, high-gain, and broadband TAs is of significant importance and holds great promise for advancing THz communication technology.

In this study, we present a novel TA design based on valley TPCs, which addresses key challenges in THz communication systems. Our design demonstrates high efficiency, broad bandwidth, and robustness to fabrication defects, offering significant advancements for practical engineering applications. To achieve these goals, we implement a comprehensive design and optimization process as follows. Firstly, valley TPCs are utilized as the foundational platform, incorporating line defects to design both the TW and the radiation surface. Precise calculations of the propagation constant and radiation direction are validated through simulations, confirming frequency-scanning capabilities. Secondly, we validate the seamless integration of the transverse electric and magnetic (TEM) horn antenna with the TA, demonstrating its ability to shape the radiation beam. By loading horn antennas with aperture angles of 30°, 40°, and 50°, we examine how the antenna's radiation pattern and performance parameters vary with the aperture angle, achieving a pencil-shaped beam ideal for THz communication systems. Thirdly, we verify the robustness of the TA's transmission and radiation characteristics when subjected to fabrication defects. Minor imperfections in the fabrication process are found to have negligible impact on the antenna's overall performance. Finally, the TA operates within the THz band range, with its central frequency located near the 0.410 THz atmospheric window. The proposed TA operates within the frequency range from 0.382 to 0.426 THz, achieving a peak realized gain of 21.7 dBi, an aperture efficiency of 63.7%, and a total efficiency exceeding 80%, with a maximum value to 95%. The radiation direction varies between 40° and 70° within the operating frequency range in the H-plane. Compared to existing end-fire and edge-emitting TAs, the proposed design outperforms in gain, efficiency, and half-power beamwidth (HPBW), while also demonstrating the inherent advantages of TAs over conventional designs, including defect robustness, simplified beam-shaping as well as radiation design. This design underscores the distinctive advantages of TPCs in antenna engineering and offers valuable insights for advancing their applications in communication technologies.

2. Design and optimization

2.1. Topological platform of unit cells and waveguides

The domain walls formed by TPCs with contrasting topological properties enable the efficient transmission of EM waves. In this study, we selected a pair of TPCs with opposite valley Chern numbers at energy bands. Based on the bulk-edge correspondence principle, edge state modes are predicted to emerge between these TPCs [23, 37].

The rhombic TPC unit cell consists of two hollow silicon pillars sandwiched between metal plates on the upper and lower surfaces, each with a height of $h = 190\,\mu$m, as shown in figures 1(a) and (b). In figure 1(a), the orange sections represent the silicon pillars, while the gray portions denote the metal plates. The silicon pillar has a relative permittivity of $\varepsilon_r = 11.7$ and a conductivity of $\sigma = 2.5 \times 10^{-4}$ S m^{-1}. The red rhombus outlines the unit cell, and the red hexagon indicates the Wigner-Seitz cell in figure 1(b). The lattice constant is $a = 240\,\mu$m, and the distance from the center of each silicon pillar to the geometric center of the Wigner–Seitz cell is $L = \sqrt{3} \cdot a/3$, which corresponds to the side length of the Wigner–Seitz cell. The inner radius of the hollow silicon pillar is $r = 25\,\mu$m, with outer radii defined as $R_1 = 2 \times r = 50\,\mu$m and $R_2 = 1.6 \times r = 40\,\mu$m, as shown in figure 1(a). In the case of inversion symmetry ($R_1 = R_2 = 2 \times r = 50\,\mu$m), the TPC exhibits a hexagonal symmetry C_6 . This symmetry gives rise to a pair of degenerate Dirac points at the valleys K and K'

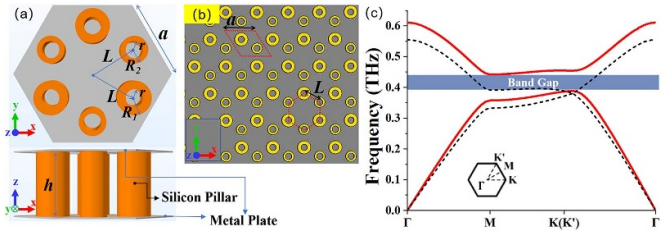

Figure 1. (a) Geometry of TPC, where the orange sections represent the silicon pillars and the gray areas denote the metal plates. (b) Top view of the TPCs with the upper metal plate removed for clarity. The red rhombus shows the unit cell of the TPC, while the red hexagon marks the Wigner–Seitz cell. (c) Energy band diagram of TPC. The red solid lines indicate the energy bands when the Dirac point is opened, while the black dashed lines represent the bands when the Dirac point is closed.

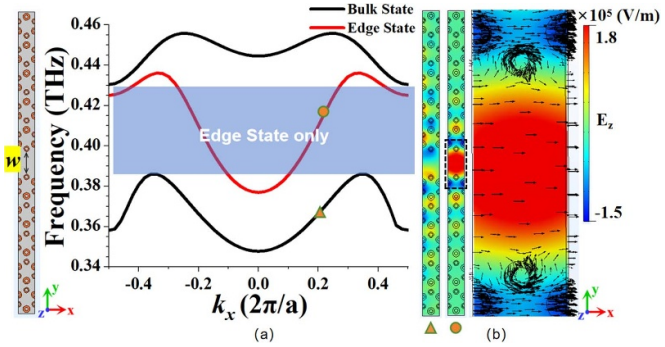

Figure 2. Structure, energy band and eigen mode profiles of the supercell with line defect. (a) Energy band diagram: the red line represents the edge state mode and the black lines denote the bulk state modes. The blue-shaded region highlights the frequency range where only the edge state mode exists. (b) Distribution of $\mathbf{E}_z$ in the supercell at $k_x = 0.2 \times (2\pi/a)$, along with the detailed profile of Poynting vector, depicted with black arrows.

in the band diagram, occurring at 0.38 THz, as indicated by the black dotted line in figure 1(c). Breaking the symmetry C_6 by varying the outer radii of the silicon pillars transforms the TPC into a C_3-symmetric structure. This modification induces the opening of the Dirac point, generating an energy band gap within the frequency range of 0.38 to 0.44 THz, as shown by the red solid lines. The berry curvature of the TPC is localized in the valleys K and K' within the same band, exhibiting opposite signs. From the Berry curvatures in the valleys, the half-integer Valley Chern numbers are determined: $C_K = $ -1/2 and $C_{K'} = 1/2$ in the first band and $C_K = 1/2$ and $C_{K'} = $ -1/2 in the second band.

The topological supercell was designed on the basis of the previously described TPC, incorporating an airline defects layer positioned along the domain wall. The width of the line defects is $w = 2 \times L$, as shown in figure 2(a). The energy band diagram of the supercell illustrates that the edge state operates within the frequency range from 0.382 to 0.434 THz, where k_x denotes the component of the wave vector $\vec{K}$ in the x-direction. The red line depicts the edge state modes, while the black lines represent the bulk state modes. For improved clarity, certain bulk state modes have been omitted. The eigen modes display in figure 2(b) illustrate that, during edge state propagation, energy is predominantly confined within the line defects governed by domain walls. The black arrows indicate the Poynting vector. The electric field $\mathbf{E}_z$ is oriented perpendicular to the xoy-plane and the magnetic field $\mathbf{H}_{\parallel}$ is parallel to the xoy-plane. One the other hand, during bulk state propagation, energy disperses throughout the supercell, inhibiting focused energy transmission.

Incorporating line defects mitigates energy diffusion losses into adjacent TPCs and expands the energy concentration region, enabling the TW to support higher power transmission. However, overly wide line defects can weaken coupling between neighboring TPCs, narrowing the topological band gap. The selected defect width of $w = 2 \times L$ strikes a balance between preserving a broad topological bandgap and minimizing diffusion losses, as confirmed by prior studies showing its ability to offer both wider operational bandwidth and improved energy confinement [23]. For edge-emitting array antennas, TWs with line defects focus radiated energy within the leaky-wave band, enhancing radiation efficiency and minimizing transmission losses.

2.2. *Antenna structure, propagation and radiation performance*

To realize the leaky-wave antenna, we reduced the number of TPC layers on the upper side of the TW and modified the TW configuration by introducing bends. These adjustments ensure that the radiation section, oriented in the positive y-direction, exclusively comprises the leaky-wave array. Figure 3(a) shows the cross-sectional view of the internal structure of the designed TA. The radiation section consists of 26 rhombic unit cells, with a total length of $N = 26 \times a$. This length optimizes both the radiation efficiency and aperture size of the TA. A length that is too short can result in incomplete radiation, thereby reducing efficiency. In contrast, an excessive length may reduce the aperture efficiency. We adjusted the radiation section length N to $24 \times a$ and $28 \times a$, resulting in total efficiencies of 87.4% and 92.4% at 0.410 THz, respectively, both lower than the efficiency of 93.6% achieved when $N = 26 \times a$. The rectangular waveguides were connected to the TA ports using wedge-shaped silicon converters, enabling feeding through the waveguides, as shown in figure 3(c). The rectangular waveguides measure $864\,\mu\text{m} \times 432\,\mu\text{m}$ in aperture size. The wedge-shaped converter has a length of $Q = 1920\,\mu$m, a width of $W = 208\,\mu$m, and a height of $190\,\mu$m, which aligns with the height of the silicon pillars in the TPC. When the TA is excited from the port, EM energy is coupled into the TW via the wedge-shaped converter. Figure 3(e) shows the S_{11} and S_{21} parameters of the TA. The S_{11} parameter demonstrates a return loss below -10 dB, indicating minimal reflection, while the S_{21} parameter confirms that most energy is radiated into free space.

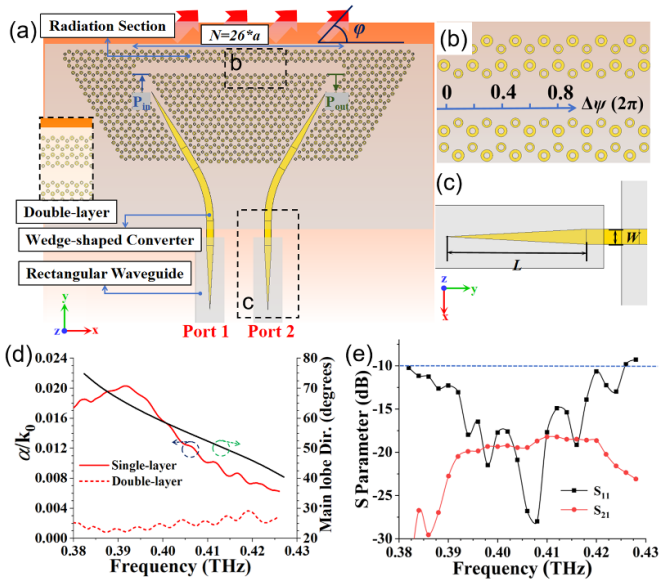

Figure 3. (a) Structural geometry of the TA. The red arrows indicate the approximate radiation direction (ϕ) when port 1 is excited. (b) Phase (ψ) variation along the x-direction within the radiation section at 0.409 THz, showing a phase change ($\Delta\psi$) of 0.2 cycle per lattice constant. (c) Geometry of the wedge-shaped converter, with dimensions of length $Q = 1920\,\mu$m, width $W = 208\,\mu$m, and height $H = 190\,\mu$m. (d) Leakage rate and theoretical variation of the main lobe direction with frequency. The energy flow entering and exiting the radiation section is determined by integrating the Poynting vector across the blue and green lines, respectively. (e) Simulated S parameters of the TA.

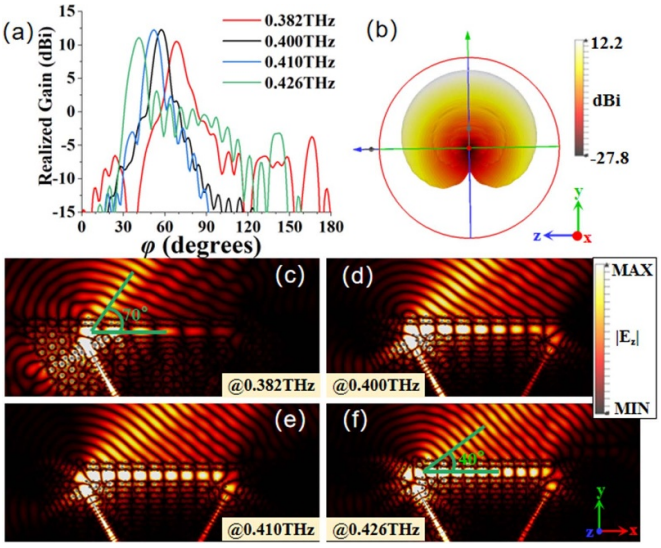

Figure 4. (a) One-dimensional far-field radiation patterns of the antenna in the H-plane (xoy-plane) at 0.382, 0.400, 0.410, and 0.426 THz. (b) Three-dimensional far-field radiation pattern of the antenna at 0.400 THz in the E-plane. (c)–(f) Electric field distribution near the radiation section of the TA in the H-plane at 0.382, 0.400, 0.410, and 0.426 THz, respectively, when port 1 is excited.

Figure 3(b) provides the phase (ψ) variation along the positive x-direction within the radiation section at 0.409 THz, where the phase shift by 0.2 cycle per a. As shown in figure 2, at 0.409 THz, the corresponding $k_x = 0.2 \times (2\pi/a) \approx 5236\,\mathrm{rad\,m^{-1}}$. The propagation phase constant, $\beta(\omega)$, of the antenna is expressed as $\beta(\omega) = k_x(\omega)$. Therefore, the main lobe direction of the TA can be calculated using the equation:

$$\phi_{\mathrm{main}} = \cos^{-1}\left[-\frac{\beta(\omega)}{k}\right] = \cos^{-1}\left[-\frac{k_x\lambda}{2\pi}\right]. \qquad (1)$$

In equation (1), k represents the wavenumber in the radiation section, which is equal to $2\pi/\lambda$. Equation (1) calculates the main lobe direction for edge-emitting arrays, allowing the variation in the antenna array's main lobe direction with frequency changes to be determined. The result is shown in figure 3(d), where the radiation direction of the TA varies within a scanning range of $\phi = 40^\circ$ to 70° as the frequency changes. Subsequent simulations show that the observed variation in the main lobe direction closely matches the theoretical predictions.

To obtain the leakage rate (α) of the TA, the surface integral of the Poynting vector was evaluated at both ends of the radiation section. This calculation provided the input energy P_{in} and the output energy P_{out} of the radiation section. The leakage rate α was then derived using the following definition [39, 45]:

$$\mathrm{P}(x) = \mathrm{P}(0)\exp\left[-2\int_0^x \alpha(\zeta)\,\mathrm{d}\zeta\right]. \qquad (2)$$

A uniform leakage rate is assumed across each unit cell of the TA. Under this assumption, $P(0) = P_{\mathrm{in}}$ and $P(x = N) = P_{\mathrm{out}}$, allowing the leakage rate to be determined, as presented in figure 3(d). To verify the impact of the number of TPC layers on the leakage rate, calculations were performed for radiation sections consisting of single-layer and double-layer TPCs. It is observed that increasing the number of TPC layers significantly reduces the leakage rate, attributed to enhanced topological protection. Consequently, a single layer of TPCs is selected for the optimized configuration. In figure 3(d), the left axis corresponds to leakage rate, while the right axis corresponds to the theoretical variation in the main lobe direction with frequency.

Figure 4(a) shows the one-dimensional far-field radiation patterns of the TA across different frequencies, illustrating the variation in the main lobe radiation direction with frequency. Figures 4(c)–(f) display the radiation electric field distribution of the TA at 0.382, 0.400, 0.410, and 0.426 THz, respectively, clearly demonstrating the frequency-dependent variation in radiation direction. Specifically, the radiation angles in figures 4(c) and (f) indicate that the radiation direction is 70° at 0.382 THz and shifts to 40° at 0.426 THz, aligning well with the theoretical predictions presented in figure 3(d).

Additionally, figure 4(b) illustrates the three-dimensional radiation pattern of the TA in the E-plane at 0.400 THz, clearly indicating that the TA generates a fan-shaped beam in the

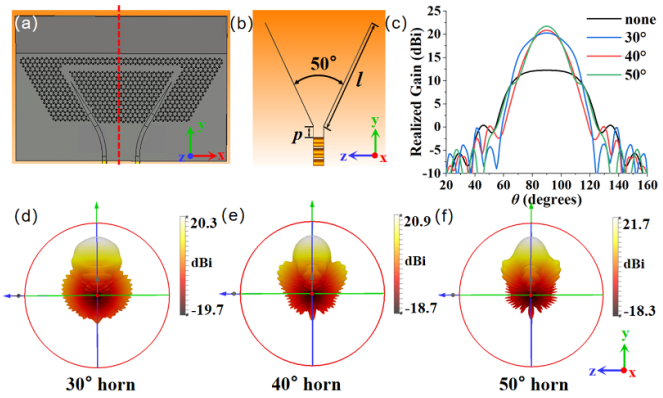

Figure 5. (a) and (b) Structural configurations of the TA integrated with a straight TEM horn antenna featuring an aperture angle of 50°. (c) Far-field radiation patterns of TAs with different horns in the E-plane. (d)–(f) Three-dimensional far-field radiation patterns of the TAs in the E-plane, corresponding to horn antennas with aperture angles of 30°, 40°, and 50°, respectively.

plane. To enhance the antenna gain and convert the fan-shaped beam into a pencil beam to meet the needs of different application scenarios, TEM horn antennas were integrated into the radiation section, enabling precise control over the beam shape.

2.3. Loading TEM horn antennas

To enhance the gain of the TA and transform the beam in the E-plane from a fan-shaped to a pencil-shaped profile, TEM horn antennas were integrated into the radiation section of the TAs. This approach demonstrates the effective impedance matching between the parallel-plate structure of the TA and the TEM horn antenna, achieved by expanding the aperture to improve gain. For comparative analysis, three TEM horn antennas with aperture angles of 30°, 40° and 50° were designed and evaluated.

The structures and radiation patterns of the proposed TAs are illustrated in figure 5. Figures 5(a) and (b) show the configurations of the TAs integrated with a TEM horn featuring an aperture angle of 50°. The metal plates of the TEM horn have a length of $l = 2120\,\mu$m, with a separation distance of $p = a$ at the connection line to the nearest TPC. To emphasize beam-shaping capabilities of the horn antenna in the E-plane, figure 5(c) presents the one-dimensional directional patterns of the four structures at 0.410 THz. As depicted, incorporating the TEM horn antenna not only narrows the main beam lobe, converting the fan-shaped beam into a pencil beam, but also enhances the antenna gain, achieving a maximum of 21.7 dBi. Figures 5(d)–(f) illustrate the three-dimensional far-field radiation patterns in the E-plane for the TA with different TEM horn antennas, clearly demonstrating the impact of the horn antennas on beam-shaping.

Figure 6(a) presents the radiation cross-section of the TA in the *yoz*-plane without a TEM horn antenna. Figures 6(b)–(d) illustrate the radiation interface diagrams of three horn antennas with different apertures sizes. In these configurations, EM waves propagate as TEM waves and are radiated into the space

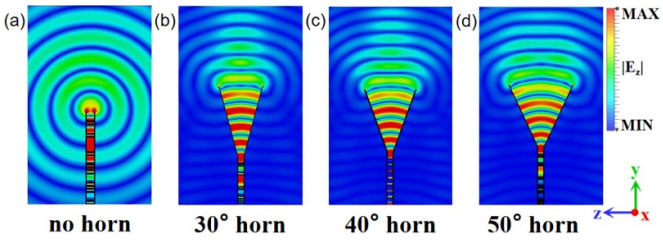

Figure 6. Cross-section views along the red line in figure 5(a), illustrating the radiation interface diagrams of TAs in the E-plane with different horn antennas: (a) without a horn, (b) with a 30° horn, (c) with a 40° horn, and (d) with a 50° horn.

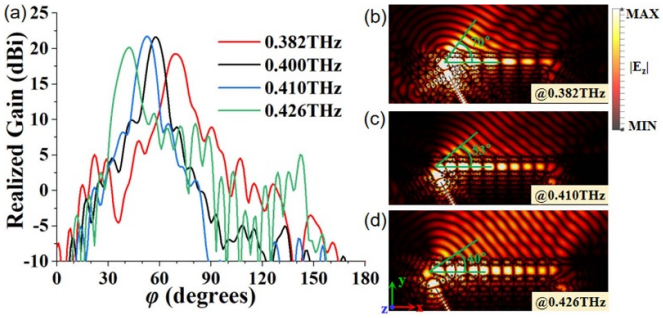

Figure 7. (a) One-dimensional far-field radiation patterns of the TA equipped with a straight TEM horn antenna with a 50° aperture in the H-plane (*xoy*-plane) at 0.382, 0.400, 0.410, and 0.426 THz. (b)–(d) Electric field distributions near the radiation section of the TA in the H-plane at 0.382, 0.410, and 0.426 THz when port 1 is excited.

through the horn structures. As shown in figure 6, the different aperture angles of the antennas affect the propagation of the waves, leading to variations in beam shape.

Figure 7(a) demonstrates the frequency-scanning capability of the TA integrated with a TEM horn antenna, confirming that integration of the TEM horn does not affect the inherent frequency-scanning characteristics of the TA. Figures 7(b)–(d) present the radiation electric field distribution of the TA in the H-plane (*xoy*-plane) at 0.382, 0.410, and 0.426 THz, respectively, clearly indicating that the radiation direction changes with frequency. These results validate the performance enhancement achieved by integrating the TEM horn antenna with the designed TA, confirming the feasibility and effectiveness of this integration. The TEM horn antenna offers additional degrees of freedom for future optimization–not only through aperture angle variation, as explored in this study, but also by adjusting the horn length and taper profile.

2.4. Verification of defect and environmental robustness

As discussed previously, TWs are renowned for their defect robustness, maintaining stable transmission properties even in the presence of manufacturing defects. To assess the defect robustness of the topological structure utilized in our designed TA, we introduced three common defects into the TA structure. For clarity, we present all three defects within a single schematic diagram, as shown in figure 8(a). The three defects

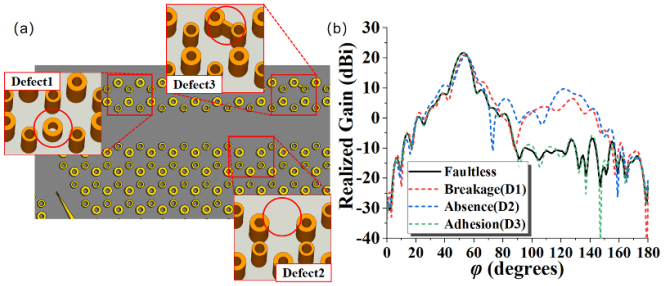

Figure 8. (a) Structural diagram of the TA with defects: Defect 1 represents silicon pillar breakage, Defect 2 corresponding to the absence of silicon pillars, and Defect 3 denotes the adhesion of fused silicon pillars. (b) One-dimensional far-field radiation patterns in the E-plane for TAs with and without defects. These TAs are equipped with TEM horn antennas featuring a 50° aperture angle, operating at 0.410 THz and are excited via port 1.

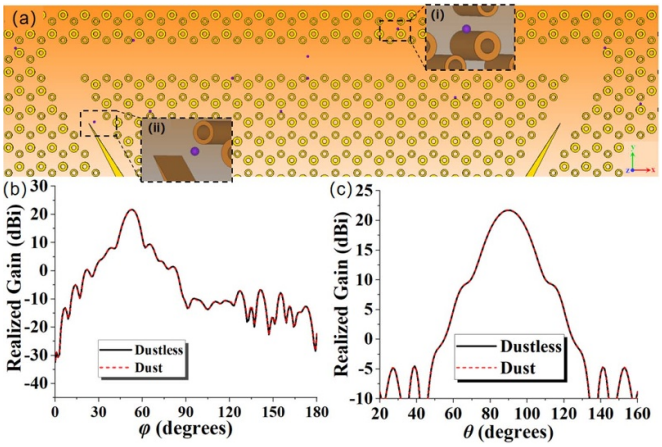

Figure 9. Antenna structure and simulation results with added dust for the case of a 50° TEM horn operating at 0.41 THz. (a) Schematic of the structure with dust particles: (i) particles adhered to the middle of the silicon pillars ($z_{c1} = 95\,\mu$m), and (ii) placed near the bottom metal plate ($z_{c2} = 15\,\mu$m). (b) Far-field radiation patterns in the H-plane. (c) Far-field radiation patterns in the E-plane.

introduced are silicon pillar breakage, absence of silicon pillars, and adhesion of fused silicon pillars, labeled as Defect 1, 2, and 3, respectively, in figure 8(a).

Figure 8(b) shows the one-dimensional far-field radiation patterns for TAs in H-plane (*xoy*-plane) with the three types of defects, operating at 0.410 THz. A comparison with a faultless TA reveals that TAs with Defects 1, and 2, which disrupt the overall array structure, still achieve high radiation efficiency and maintain a significant gain. However, the disruption of the radiation section array results in the emergence of new side lobes. In contrast, Defect 3 preserves a far-field radiation pattern similar to that of the faultless antenna, without introducing additional side lobes.

Defect robustness is a critical feature of TWs, ensuring stable transmission even in the presence of structural imperfections. For leaky-wave TAs, defect robustness helps maintain overall radiation intensity despite such defects. However, structural changes caused by defects can affect various performance parameters, including the main lobe width and the side lobe suppression. While topological propagation ideally bypasses defects, their impact on the radiation pattern remains unavoidable. Therefore, careful consideration of defect immunity is essential when designing TPC-based leaky-wave arrays.

Beyond structural defects, antennas in practical scenarios often face environmental challenges, such as airborne dust. Although encapsulation and radome protection typically prevent exposure to high concentrations of large particles (e.g. sandstorms), occasional contact with smaller airborne contaminants remains possible. To assess the resilience under such conditions, we simulated the presence of typical airborne particles within the antenna structure, as illustrated in figure 9.

Specifically, polyimide spheres with a relative permittivity of 3.5 and a diameter of 30 μm were used to mimic typical airborne polymer-based particles. These particles were placed either (i) adhered to the middle of the silicon pillars (with a center height of $z_{c1} = 95\,\mu$m), or (ii) deposited near the bottom metal plate (center height of $z_{c2} = 15\,\mu$m), as illustrated by the purple spheres in figure 9(a). The one-dimensional far-field radiation patterns at 0.41 THz, shown in figures 9(b) and (c), reveal that these dielectric particles have minimal influence on radiation characteristics. The beam shape, peak gain, and side lobe level (SLL) remain virtually unchanged, demonstrating strong environmental tolerance of the TA.

This robustness arises primarily from two factors: (i) the particles possess low permittivity, close to that of air, which introduces minimal disruption to the field distribution; and (ii) their size is electrically small, approximately one-tenth to one-twentieth of the wavelength, which limits their influence on EM wave propagation.

3. Analysis and evaluation

To comprehensively evaluate the TA performance, we extracted multiple key parameters through simulation calculations to systematically analyze its radiation characteristics and structural adaptability. First, by comparing the multi-frequency E-plane radiation patterns under different TEM antenna loadings, the variation of gain with respect to frequency and direction was investigated. Simultaneously, quantitative analysis of aperture efficiency and total efficiency revealed the influence of the TEM antenna's aperture angle on energy distribution and radiation efficiency. Furthermore, through the combined characterization of the HPBW and SLL, the beam shape and directivity were quantified, while the antenna's spatial resolution were also assessed. These parameters collectively establish a multidimensional evaluation framework, providing critical theoretical insights and data support for optimizing antenna design and practical applications.

All findings presented in this work are derived from numerical simulations. The simulations of the TAs were performed using Computer Simulation Technology (CST)

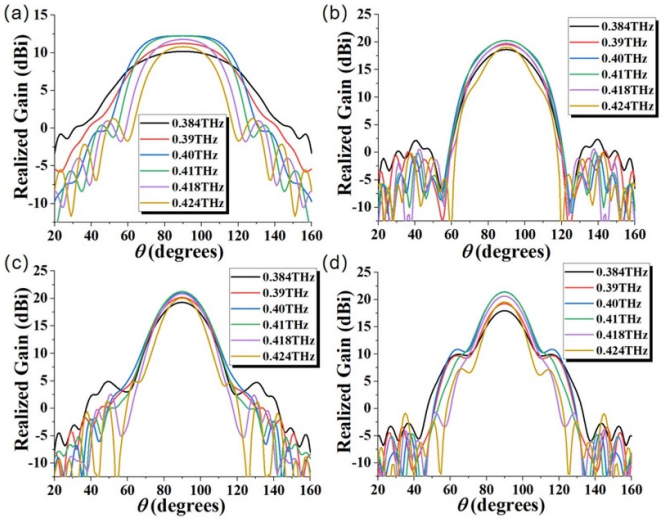

Figure 10. One-dimensional far-field radiation patterns of the TA in the E-plane for various aperture configurations: (a) without horn loading, (b) with a 30° horn, (c) with a 40° horn, and (d) with a 50° horn.

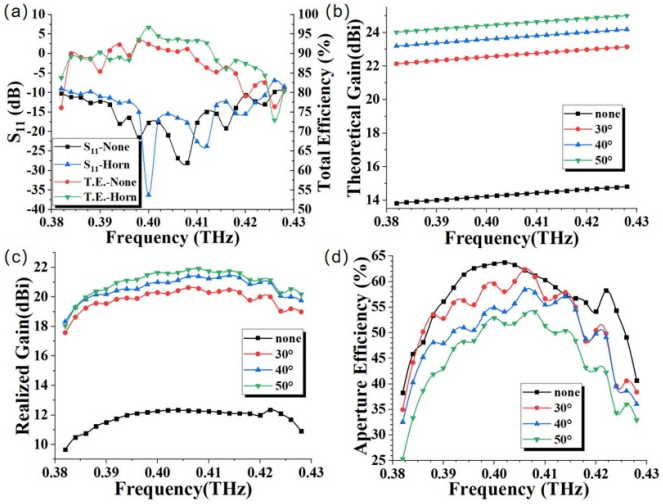

Figure 11. Simulated efficiency and gain characteristics of the TA: (a) S_{11} parameter and total efficiency, (b) theoretical gain, (c) realized gain, and (d) aperture efficiency for various aperture configurations across the operating frequency range.

software, which employed the finite-difference time-domain algorithm as the core computational approach. Additionally, the leakage rates of the TAs and the energy band structures of the topological supercells were obtained through simulations conducted with COMSOL Multiphysics software. Both CST and COMSOL are widely recognized robust tools, renowned for their high accuracy and precision in EM simulations, lending reliability to the presented results. The calculations of Berry curvature and valley Chern numbers were implemented using MATLAB.

3.1. Far-field radiation patterns and total efficiency

The far-field radiation patterns of the proposed TAs in the E-plane at different frequencies are presented in figure 10. The maximum gain of all TA models is centered around 0.400 and 0.410 THz, with a gain reduction of no more than 3 dBi at the critical frequencies of 0.384 and 0.424 THz. Notably, the TA with a 50° aperture angle generates two side lobes in its radiation pattern, whereas the side lobes in other models are less pronounced.

Figure 11(a) shows the total efficiency of the TA with and without the horn antenna loaded. Additionally, the S_{11} parameter is introduced in the same figure to illustrate the influence of return loss on the total efficiency. The left axis corresponds to the S_{11} parameter, while the right axis represents the total efficiency. Around 0.400 and 0.410 THz, the TA achieves higher total efficiency, with the horn-loaded configuration reaching over 95%. At the critical frequencies of the topological edge states (0.382 and 0.424 THz), an increase in return loss leads to a slight reduction in total efficiency. Nonetheless, both parameters remain within acceptable ranges. Given the minimal impact of the horn's aperture on the antenna's total efficiency, the figure focuses solely on simulation results for the horn-loaded and non-horn-loaded configurations.

3.2. Gain and aperture efficiency

Aperture efficiency serves as a crucial metric for assessing antenna performance, yet it has received limited attention in prior leaky-wave TA designs. To evaluate the aperture efficiency, we compute the realized gain and theoretical gain derived from the physical aperture, as depicted in figures 11(b) and (c). At 0.410 THz, the length N of the radiation section is considered the aperture length, giving the antenna's long side length L_λ as 8.32λ . For the hornless configuration and horn antennas with aperture angles of 30°, 40°, and 50°, the corresponding widths W_λ are 0.26λ, 1.76λ, 2.24λ, and 2.71λ, respectively. Based on these dimensions, the maximum theoretical gains are calculated as 14.4, 22.8, 23.8, and 24.6 dBi, respectively,

$$G = \frac{4\pi A_e}{\lambda^2}, \tag{3}$$

$$\eta_a = \frac{G}{G_{\max}} = \frac{A_e}{A}. \tag{4}$$

Equation (3) defines the relationship between aperture and gain, while equation (4) outlines the method for calculating aperture efficiency. Using these equations, the aperture efficiency of different antennas can be determined. In the equations, G represents the antenna gain, A_e denotes the effective aperture, η_a is the aperture efficiency, $G_{\max}$ indicates the maximum theoretical gain, and A refers to the physical aperture. The results depicted in figure 12(d) show that the TA without a horn antenna achieves the highest aperture efficiency, reaching 63.7% at 0.402 THz. The inverse relationship between gain and aperture efficiency highlights a fundamental design compromise: larger horns improve gain but reduce energy concentration within the aperture. In the current design, the horn length l (defined by the length of the metal plates)

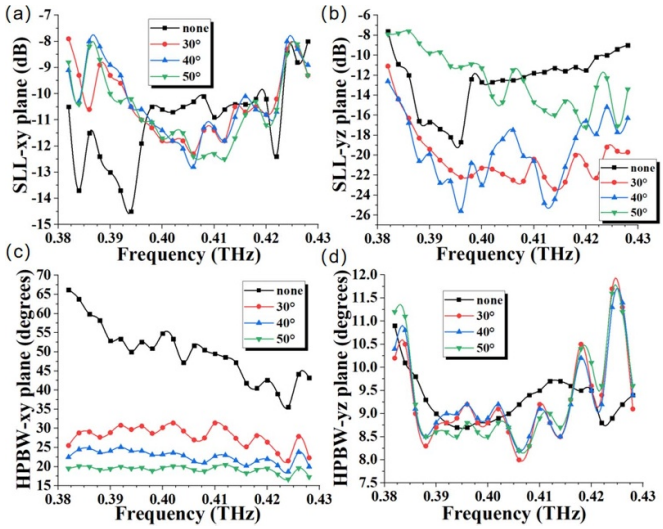

Figure 12. SLL and HPBW of TAs with different aperture configurations in the H-plane and the E-plane: (a) SLL in the H-plane, (b) SLL in the E-plane, (c) HPBW in the H-plane, and (d) HPBW in the E-plane.

Table 1. Comparison among the proposed antennas with references.

References	BW (%)	Freq. (GHz)	Size (λ_0)	G (dBi)	HPBW (°)	T.E. (%)
[38]	13	18.75	/	19.5	5	/
[39]	6	6.55	11.46×0.55	/	4.5	89
[37]	9.2	325	/	12.2	25*	/
[42]	7.6	327.5	/	12.3	/	/
[46]	15.7	11.4	11.4×0.88	19.8	24	/
[47]	1.8 & 1.6	3.6 & 4.9	4.26×0.65	14.1	/	80
[48]	50	5	8.67×1.32	13.59	/	67
[49]	143	1500	4.43×2.86	19.76	/	88
Prop.	10.4	403	8.32×2.2	21.7 ↑	9 ↑	93 ↑

Note: Values marked with * indicate that the data provided is HMAW (half-maximum-gain angle width) rather than HPBW. BW stands for bandwidth, G represents gain, T.E. denotes total efficiency, and HPBW refers to HPBW.

is fixed. However, additional simulations confirm a consistent trend: when the aperture angle is held constant, increasing l leads to higher realized gain but reduced aperture efficiency. These interrelated trade-offs–among horn geometry, gain, and efficiency–should be considered carefully when optimizing horn antennas for beam-shaping applications.

3.3. Side lobe level and HPBW

The SLL and HPBW are fundamental parameters for evaluating beam performance, particularly in the design of leaky-wave antennas. Figure 12 illustrates a detailed analysis of the SLL and HPBW of the proposed TA in both the H-plane (*xoy*-plane) and the E-plane, providing a comprehensive assessment of its beam characteristics.

Regarding the SLL, in the E-plane, the 30° and 40° horn antennas demonstrate a significant reduction in SLL, effectively concentrating energy within the main lobe. In contrast, the SLL of the 50° horn antenna is comparable to that of the hornless design, as shown in figure 12(b). However, the positions of the side lobes differ, warranting further discussion in conjunction with figure 11. In the H-plane, all configurations achieve an SLL below −10 dB near the center frequency, ensuring satisfactory suppression of side lobes, as shown in figure 12(a).

In terms of HPBW, the TA without a horn exhibits a significantly wider HPBW in the E-plane due to the absence of beam control mechanisms. For horn-loaded configurations, an increase in horn aperture angle results in a reduction of HPBW, aligning well with conventional antenna theory. In the H-plane (*xoy*-plane), the HPBW remains relatively stable, ranging from 8° to 9.5° within the frequency range from 0.390 to 0.418 THz. From a practical perspective, reducing the length of the array or decreasing the number of unit cells in the radiation section can increase the HPBW in the H-plane.

3.4. Comparison

Table 1 compares the parameters of the proposed design with those of several references, focusing on the first four antennas classified as TA. The edge-emitting antenna presented in [38] achieves high gain and supports frequency-scanning; however, it suffers from higher losses and larger dimensions compared to the proposed design. On the other hand, the broadside radiation antenna in [39] demonstrates commendable total efficiency but depends on a Chern TPC structure, which requires

an external bias magnetic field. Meanwhile, the end-fire antennas reported in [37, 42], operating in the THz band, are limited by their small apertures, making them more suitable for short-range, high-directionality communication scenarios. In comparison, the proposed edge-emitting TA features a wider HPBW than the existing edge-emitting TAs in [38, 39], while maintaining a comparable gain without significant performance degradation.

The antennas presented in [46–48] represent different types of leaky-wave designs and are distinct from TAs. The antenna proposed in [46] is comparable to proposed design but lacks frequency-scanning capability and shows significant gain variation across the frequency range. The dual-band antenna in [47] achieves high aperture efficiency but suffers from a narrow bandwidth. Meanwhile, the circularly polarized end-fire antenna in [48] offers a broader bandwidth but at the cost of reduced aperture efficiency and total efficiency. Sharma and Kumar [49] proposed an ultra-wideband THz dual-ridged pyramidal horn antenna. However, due to its complex structural design and the lack of high-power excitation sources, this approach faces potential risks in practical applications, including insufficient fabrication precision and limited excitation power.

In contrast, the proposed edge-emitting TA demonstrates superior total efficiency, gain, and aperture efficiency. These advantages underscore the importance of advancing research on leaky-wave TAs, particularly edge-emitting configurations, and highlight the substantial reference value of our design within this domain.

4. Conclusion

This study introduces a leaky-wave TA specifically designed for optimal performance in THz communication, operating within the frequency range from 0.382 to 0.426 THz. The design incorporates hollow silicon pillars sandwiched between parallel plates to form a TPC unit cell, which is subsequently used to construct a topological radiation section. Through theoretical analysis of the energy bands of the supercells, the phase gradient properties of the TA were verified, demonstrating its frequency-scanning capability. The antenna achieves high gain and total efficiency, with TEM horn antennas effectively shaping the radiation pattern into a pencil beam. Future designs could explore hybrid horn geometries or dynamic reconfiguration to further reconcile gain and efficiency. Simulations further validate the robustness of the TA's radiation and transmission performance against fabrication defects. Additionally, the design supports direct feeding via rectangular waveguides, facilitated by silicon wedge-shaped converters for seamless integration. These features make it possible for the proposed TA to be used in radar systems, demonstrating its potential in practical engineering applications.

Data availability statement

All data that support the findings of this study are included within the article (and any supplementary files).

Acknowledgment

This work was supported in part by the Shaanxi S&T Innovation Team under Grant No. 2023-CX-TD-03.

ORCID iDs

Haolong Wang https://orcid.org/0009-0009-9837-3377
Hongyu Shi https://orcid.org/0000-0002-0137-4421
Wei E I Sha https://orcid.org/0000-0002-7431-8121
Zhihao Lan https://orcid.org/0000-0002-1322-5925
Fei Gao https://orcid.org/0000-0001-9928-9390
Xiaoming Chen https://orcid.org/0000-0003-3151-1690
Anxue Zhang https://orcid.org/0000-0002-3254-6679

References

[1] Lu L, Joannopoulos J D and Soljačić M 2014 Topological photonics *Nat. Photon.* **11** 821–9
[2] Khanikaev A B and Shvets G 2017 Two-dimensional topological photonics *Nat. Photon.* **11** 763–73
[3] Zhan M, Wu J, Li Y, Xu G and Zhu Y 2024 An adaptive nonlinear phase error estimation and compensation method for terahertz radar imaging system *IEEE J. Miniaturization Air Space Syst.* **5** 108–16
[4] Liu J, Dai J, Chin S L and Zhang X-C 2010 Broadband terahertz wave remote sensing using coherent manipulation of fluorescence from asymmetrically ionized gases *CLEO/QELS: 2010 Laser Science to Photonic Applications* pp 1–2
[5] Nagatsuma T, Ducournau G and Renaud C 2016 Advances in terahertz communications accelerated by photonics *Nat. Photon.* **10** 371–9
[6] Yang Y, Yamagami Y, Yu X, Pitchappa P, Webber J, Zhang B, Fujita M, Nagatsuma T and Singh R 2020 Terahertz topological photonics for on-chip communication *Nat. Photon.* **14** 446–51
[7] Gu Q J 2015 Thz interconnect: the last centimeter communication *IEEE Commun. Mag.* **53** 206–15
[8] Rappaport T S, Xing Y, Kanhere O, Ju S, Madanayake A, Mandal S, Alkhateeb A and Trichopoulos G C 2019 Wireless communications and applications above 100 GHz: Opportunities and challenges for 6G and beyond *IEEE Access* **7** 78729–57
[9] Ren H *et al* 2024 Terahertz flexible multiplexing chip enabled by synthetic topological phase transitions *Natl Sci. Rev.* **11** nwae116
[10] Cheng X, Jouvaud C, Ni X, Mousavi S H, Genack A Z and Khanikaev A B 2016 Robust reconfigurable electromagnetic pathways within a photonic topological insulator *Nat. Mater.* **15** 542–8
[11] Han J, Liang F, Zhao Y, Liu J, Wang S, Wang X, Zhao D and Wang B-Z 2024 Valley kink states and valley-polarized

chiral edge states in substrate-integrated topological photonic crystals *Phys. Rev. Appl.* **21** 014046
[12] Nivedan A and Kumar S 2023 Excitation wavelength-dependent ultrafast thz emission from surface and bulk of three-dimensional topological insulators *J. Phys. D: Appl. Phys.* **56** 255101
[13] Singh S, Bisharat D and Sievenpiper D 2021 Topological antennas: aperture radiators, leaky-wave surfaces and orbital angular momentum beam generation *J. Appl. Phys.* **130** 023101
[14] Lumer Y and Engheta N 2020 Topological insulator antenna arrays *ACS Photonics* **7** 2244–51
[15] He L, Lan Z, Yang Y, Ren Q, You J W, Sha W E I, Liang W and Yao J 2024 Wavelength division multiplexing based on the coupling effect of helical edge states in two-dimensional dielectric photonic crystals *Opt. Express* **32** 11259–70
[16] Lu J, He L, Addison Z, Mele E J and Zhen B 2021 Floquet topological phases in one-dimensional nonlinear photonic crystals *Phys. Rev. Lett.* **126** 113901
[17] Luo L, Ye L, He H, Lu J, Ke M and Liu Z 2023 Experimental observation of the topological interface state in a one-dimensional waterborne acoustic waveguide *Phys. Rev. Appl.* **20** 044008
[18] Jeon S and Kim Y 2022 Two-dimensional weak topological insulators in inversion-symmetric crystals *Phys. Rev. B* **105** L121101
[19] Zhou Y-C, Lai H-S, Xie J-L, Sun X-C, He C and Chen Y-F 2023 Magnetic corner states in a two-dimensional gyromagnetic photonic crystal *Phys. Rev. B* **107** 014105
[20] Wang Z, Liu D, Teo H T, Wang Q, Xue H and Zhang B 2022 Higher-order dirac semimetal in a photonic crystal *Phys. Rev. B* **105** L060101
[21] Chen M L N, j. Jiang L, Lan Z and Sha W E I 2020 Pseudospin-polarized topological line defects in dielectric photonic crystals *IEEE Trans. Antennas Propag.* **68** 609–13
[22] Xue H, Yang Y and Zhang B 2021 Topological valley photonics: physics and device applications *Adv. Photonics Res.* **2** 2100013
[23] Li B, Shi H, Sha W E, Yi J, Li G, Zhang A and Xu Z 2022 Valley topological line-defects for terahertz waveguides and power divider *Opt. Mater.* **126** 112152
[24] He X-T, Guo C-H, Tang G-J, Li M-Y, Chen X-D and Dong J-W 2022 Topological polarization beam splitter in dual-polarization all-dielectric valley photonic crystals *Phys. Rev. Appl.* **18** 044080
[25] Xiong Z, Lin Z-K, Wang H-X, Zhang X, Lu M-H, Chen Y-F and Jiang J-H 2020 Corner states and topological transitions in two-dimensional higher-order topological sonic crystals with inversion symmetry *Phys. Rev. B* **102** 125144
[26] Tang G-H, Hong Y-L, Zhang R-L, Fan R-H, Ma Z-L, Wu X-Y, Qi D-X, Peng R-W and Wang M 2023 Adjustable topological corner states in terahertz valley photonic crystals *Phys. Rev. B* **108** 205411
[27] Zhang Z, Yang J and Lan Z 2024 Tailoring coupled topological corner states in photonic crystals via symmetry breaking induced by defects *Phys. Rev. Res.* **6** 013321
[28] Wei G, Liu Y, Liu Z, Zhang D and Xiao J 2020 Realization of hierarchical topological transitions and high-q-response corner states in second-order topological photonic crystals *J. Phys. D: Appl. Phys.* **53** 435104
[29] Li M, Liu Y, Zhou X, Du L, Li P, Tao L, Song K, Li Z and Zhao X 2024 Large-area gapped edge states in a valley photonic crystal heterostructure *J. Phys. D: Appl. Phys.* **57** 475302
[30] Chen Q, Zhang L, Chen F, Yan Q, Xi R, Chen H and Yang Y 2021 Photonic topological valley-locked waveguides *ACS Photonics* **8** 1400–6
[31] Yan S, Yang J, Shi S, Zuo Z, Wang C and Xu X 2023 Transport of a topologically protected photonic waveguide on-chip *Photon. Res.* **11** 1021
[32] Lan Z, Chen M L N, You J W and Sha W E I 2023 Large-area quantum-spin-hall waveguide states in a three-layer topological photonic crystal heterostructure *Phys. Rev. A* **107** L041501
[33] Li M X, Wang Y K, Lu M J and Sang T 2021 Dual-mode of topological rainbow in gradual photonic heterostructures *J. Phys. D: Appl. Phys.* **55** 095103
[34] Lumer Y and Engheta N 2018 Robust radiation from photonic topological insulators *2018 Conf. on Lasers and Electro-Optics (CLEO)* pp 1–2
[35] Gorlach M A, Ni X, Smirnova D A, Korobkin D, Zhirihin D, Slobozhanyuk A P, Belov P A, Alú A and Khanikaev A B 2018 Far-field probing of leaky topological states in all-dielectric metasurfaces *Nat. Commun.* **9** 909
[36] Zhang Z, Tian Y, Wang Y, Gao S, Cheng Y, Liu X and Christensen J 2018 Directional acoustic antennas based on valley-hall topological insulators *Adv. Mater.* **30** 1803229
[37] Jia R, Kumar S, Tan T C, Kumar A, Tan Y J, Gupta M, Szriftgiser P, Alphones A, Ducournau G and Singh R 2023 Valley-conserved topological integrated antenna for 100-Gbps THz 6G wireless *Sci. Adv.* **9** eadi8500
[38] Abtahi S A, Maddahali M and Bakhtafrouz A 2024 Realizable leaky wave antenna based on spin photonic topological insulators *IEEE Access* **12** 1–1
[39] Xu Z, Wang M, Fang S, Liu H, Wang Z and Sievenpiper D F 2022 Broadside radiation from chern photonic topological insulators *IEEE Trans. Antennas Propag.* **70** 2358–63
[40] Gangaraj S A H and Monticone F 2018 Topologically-protected one-way leaky waves in nonreciprocal plasmonic structures *J. Phys.: Condens. Matter* **30** 104002
[41] Wang W-Y, Ren H, Xu Z-H, Chen H, Li Y and Xu S 2024 Integrated terahertz topological valley-locked power divider with arbitrary power ratios *Opt. Lett.* **49** 5579–82
[42] Wang W, Tan Y J, Tan T C, Kumar A, Pitchappa P, Szriftgiser P, Ducournau G and Singh R 2024 On-chip topological beamformer for multi-link terahertz 6G to XG wireless *Nature* **632** 522–7
[43] Webber J, Yamagami Y, Ducournau G, Szriftgiser P, Iyoda K, Fujita M, Nagatsuma T and Singh R 2021 Terahertz band communications with topological valley photonic crystal waveguide *J. Lightwave Technol.* **39** 7609–20
[44] Cao X, Hao J, Zhao Q, Zhang F, Fan J and Dong Z 2022 Analysis of high-frequency atmospheric windows for terahertz transmission along earth-space paths *IEEE Trans. Antennas Propag.* **70** 5715–24
[45] Oliner A A and Jackson D R 2007 Leaky-wave antennas *Antenna Engineering Handbook* (McGraw-Hill)
[46] Wang K, Li Y, Liang Z, Zheng S Y and Long Y 2022 A high-gain endfire periodic leaky-wave antenna using dspsl-based rhombic element *IEEE Trans. Antennas Propag.* **70** 11109–14
[47] Li H-D and Zhu L 2022 Dual-frequency microstrip leaky-wave antenna for high-gain broadside radiation *IEEE Trans. Antennas Propag.* **70** 6560–70
[48] Wu Z, Miao Z and Deng X 2023 High-gain and wideband circularly polarized endfire leaky-wave antenna array based on the complementary dipole *IEEE Trans. Antennas Propag.* **71** 6168–72
[49] Sharma A and Kumar D 2024 Investigation of a superstrate loaded ultrawideband dual-ridged terahertz pyramidal horn antenna *IEEE Antennas Wirel. Propag. Lett.* **23** 4533–7